Coherent interactions of a fast proton with the short-range *NN* correlations in the nucleus

A. B. Larionov [1,*] and Yu. N. Uzikov [2,3,4,†]

[1] *Bogoliubov Laboratory of Theoretical Physics, Joint Institute for Nuclear Research, 141980 Dubna, Russia*

[2] *Laboratory of Nuclear Problems, Joint Institute for Nuclear Research, 141980 Dubna, Russia*

[3] *Department of Physics, Moscow State University, 119991 Moscow, Russia*

[4] *Dubna State University, 141980 Dubna, Russia*

(Received 20 November 2023; revised 29 February 2024; accepted 6 May 2024; published 3 June 2024)

Nuclear structure at short *NN* distances is still poorly understood. In particular, the full quantum structure of the nucleus with a correlated *NN* pair is a challenge to theory. So far, model descriptions have been limited to the average mean-field picture of the remaining nuclear system after removing the *NN* pair. In the recent experiment of the BM@N Collaboration at JINR [M. Patsyuk *et al.*, Nat. Phys. **17**, 693 (2021)], the reactions $^{12}\mathrm{C}(p, 2pn_s)^{10}\mathrm{B}$ and $^{12}\mathrm{C}(p, 2pp_s)^{10}\mathrm{Be}$ induced by the hard elastic *pp* scattering were studied. Here, n_s or p_s denote the undetected slow nucleon in the rest frame of ^{12}C. In contrast to the previous experiments, the residual bound nucleus was also detected which requires a new level of theoretical understanding. In the present work, we apply the technique of fractional parentage coefficients of the translationally invariant shell model to calculate the spectroscopic amplitude of the system *NN*-*B* where *B* is the remaining nuclear system. The spectroscopic amplitude enters the full amplitude of a nuclear reaction. The relative *NN*-*B* wave function is no longer a free parameter of the model but is uniquely related to the internal state of *B*. The interaction of the target proton with the *NN* pair is considered in the impulse approximation. We also include the initial- and final-state interactions of absorptive type as well as the single charge exchange processes. Our calculations are in a reasonable agreement with the BM@N data.

DOI: 10.1103/PhysRevC.109.064601

I. INTRODUCTION

Short-range *NN* correlations (SRCs) in nuclei have been the focus of experimental and theoretical studies for about three decades, see recent reviews in Refs. [1,2]. It is nowadays well established that in medium-to-heavy nuclei about 20–25 % of nucleons are in the state of SRCs. These nucleons populate the part of the nucleon momentum distribution above Fermi momentum of $\approx$250 MeV/c [3]. Most SRCs are the *pn* ones, although a fraction of *pp*-SRCs increases with missing momentum[1] at $p_{\mathrm{miss}} = 400$–800 MeV/c indicating the transition from dominating tensor to dominating repulsive scalar interaction, which follows from the analysis of the reaction $^4\mathrm{He}(e, e'pN)$ at Jefferson Laboratory [4]. This conclusion is also supported by the increasing cross-section ratio $A(e, e'pp)/A(e, e'p)$ with p_{miss} at $p_{\mathrm{miss}} = 400$–600 MeV/c, independent of the target nucleus [5].

Most experimental searches for SRCs have been carried out by detecting a scattered particle (e or p), a recoil proton, and its partner nucleon, c.f. Refs. [3–8], while the state of the residual nuclear system was not determined. Hence, the reaction products may suffer incoherent rescattering processes in the residual nucleus, leading to the distortions of their momenta and the formation of a highly excited nuclear residue, which may even be in an unbound state.

In the experiments performed at NIKHEF [9–11] and MAMI [12], the reaction $^{16}\mathrm{O}(e, e'pp)^{14}\mathrm{C}$ with production of ^{14}C in the 0^+ ground state and several excited states (2^+ at $E^* = 7.01$ and 8.32 MeV, 0^+ at $E^* = 9.75$ MeV, and 1^+ at $E^* = 11.31$ MeV) has been studied. The main idea was to use specific final states of the outgoing nucleus as a filter for various reaction processes. For example, ^{14}C in the 0^+ states associated with low recoil momentum selects the $^1S_0$ internal state of *pp*, while ^{14}C in the 1^+ state selects the ^3P states of the *pp* pair. In Ref. [11] the two independent theoretical analyses within the Pavia [13] and Gent [14] models have been performed concluding that the ground state channel is well described by introducing central SRCs. On the other hand, the 1^+ channel needs to include the intermediate Δ excitation [15], thus, clearly demonstrating the importance of the selection of the quantum state of a residual nucleus for the observation of SRCs.

In Refs. [16,17], the tensor correlations that influence the $^3S_1$ and $^3D_1$ *pn* states are found to be important for the $^{16}\mathrm{O}(e, e'pn)^{14}\mathrm{N}$ exclusive channels with production of ^{14}N in the 1^+ states. However, since the energy resolution of the neutron detector [18] turned out to be not enough to resolve the separate energy state of ^{14}N, these important theoretical predictions still remain to be confirmed by new experiments. In this sense, a more effective way to study *pn* SRCs (which

*larionov@theor.jinr.ru

†uzikov@jinr.ru

[1] The missing momentum p_{miss} is defined as the momentum of the struck proton in the nucleus rest frame before knock-out.

are more abundant as compared to the pp ones) is to use reactions in the inverse kinematics where the residual nucleus can also be detected, allowing the final state to be completely reconstructed without the need for neutron detection.

The first (almost) fully exclusive measurements of the reactions $^{12}\mathrm{C}(p, 2pn_s)^{10}\mathrm{B}$ and $^{12}\mathrm{C}(p, 2pp_s)^{10}\mathrm{Be}$ in inverse kinematics with the collision of carbon nuclei with a momentum of 48 GeV/c with a proton target were recently performed by the BM@N Collaboration at JINR [19]. The main idea was to reduce distortions of the reaction kinematics due to initial- and final-state interactions (ISI/FSI) by detecting an unbroken nucleus in the final state. This allows to extract more clean information on the genuine SRC dynamics. An important feature of this experiment is the detection of a fast residual nucleus at a finite distance from the point of interaction with the proton target. Under these conditions, residual nuclei in short-lived particle-unstable states will not reach the detector. Hence, only the ground state and low-lying excited states of the residual nucleus will contribute to the counting rate. Therefore, it is extremely important that the appropriate theoretical formalism, in addition to the correct description of the SRC pair and its motion relative to the residual nucleus, also takes into account individual transitions to low-lying excited states of the residual nucleus.

Theoretical modeling of SRCs is based on the separation of long-range mean-field interactions and (relatively) short-range residual two-body interactions, which is confirmed by microscopic calculations [20–22]. It was shown [22] that for nuclei with $A \leqslant 12$ the independent particle model (IPM) predicts the number of the NN pairs in different spin-isospin states ST with an accuracy of about 10–15 % compared with a calculation taking into account correlations. In this case, residual interactions primarily affect the internal wave function (WF) of the pair. In Ref. [20], the binding energies of s- and p-shell nuclei were well described by a simple model in which the pion-exchange spin-isospin interaction acts within NN pairs of different ST while counting of pairs in a given spin-isospin state was carried out within the IPM.

In the model of Refs. [23–25], SRCs were dynamically generated by correlation operators acting on the IPM WF. The authors showed that the correlation operators (in the two-body cluster approximation) do not affect the distribution of center-of-mass (c.m.) momenta of correlated pairs, while most of the SRCs is generated by the action of correlation operators on the NN pairs in the lowest internal state of the relative radial quantum number $n = 0$ and relative orbital momentum $l = 0$.

Another SRC model is the generalized contact formalism (GCF), see Ref. [26] and references therein. In the GCF, the total number of SRCs is included through nuclear contacts that can be extracted either from experiment [27,28] or from microscopic calculations [26,29]. Internal WFs of the NN SRCs in different spin-isospin states are zero-energy solutions of the Schrödinger equation with either phenomenological or chiral two-body interactions. The relative NN-B (i.e., the c.m.) WF of SRCs is purely phenomenological. Simulations using the GCF describe the BM@N data [19] very well, although this model does not include information about the internal WF of the residual nucleus and, therefore, implicitly gives the total production rate for all possible internal states of the residual nuclear system.

In this work, to resolve individual states of the residual nucleus, we use an approach based on the expansion of the nuclear wave function in a series of states of the translationally invariant harmonic oscillator shell model (TISM) [30]. The basic properties of this approach were formulated in Ref. [31] where the quasielastic knock-out of d, t, and α clusters from $1p$-shell nuclei by fast protons was studied. Momentum distribution of clusters in the nucleus and spectrum of excitations of the residual nucleus after fragment ejections were calculated in Ref. [31] using the shell model taking into account pair nucleon-nucleon correlations which explicitly demonstrated the importance of the fractional parentage method. Following Ref. [31] we assume that the number of SRC pairs in the nucleus and the WF of the relative motion of the NN pair with respect to the c.m. of the residual nucleus are determined by the mean field, while the high-momentum part of the internal wave function of the NN pair is governed by the short-range NN interaction. Accordingly, we use the TISM for the calculation of the spectroscopic amplitude [see Eq. (7) below] for separation of a two-nucleon cluster from the initial nucleus and of the WF of relative motion of the cluster and the residual nucleus. On the other hand, we rely on phenomenology to determine the intrinsic dynamic properties of SRC pairs. Hence, for the pn SRC pairs with $(S, T) = (1, 0)$, the internal WF at high relative momenta ($\gtrsim 0.4$ GeV/c) is identified with the free deuteron WF, while for the NN pairs with $(S, T) = (0, 1)$—with the $^1S_0$ WF of free pp scattering at zero energy.

In the TISM, the harmonic oscillator (HO) potential allows analytical calculation of the spectroscopic amplitudes and relative NN-B WFs. Residual NN interactions beyond the HO potential are taken into account by mixing the TISM configurations in the intermediate coupling scheme [31,32]. We should note here that within the TISM the type of WF of the relative motion of the cluster X and the residual nucleus B is determined by the antisymmetry property of the internal WFs of the nuclei A and B and of the cluster X. As a result, the number of the oscillator quanta n corresponding to the relative $X - B$ motion is fixed as

$$n = N_A - N_X - N_B, \tag{1}$$

where N_i is the number of oscillator quanta corresponding to the internal motion in the nucleus/cluster i ($i = A, B, X$). This "oscillator rule" is widely used in the theory of nucleon clusters in light nuclei (see, for example, Refs. [16,33]). According to this rule, when a NN pair is separated from the ground state of the ^{12}C nucleus, the relative NN-B motion has either a $2S$ or $2D$ type for the transition to the residual nucleus in the configuration s^4p^6, or $0S$ type for transition to the s^2p^8 configuration. On the contrary, within the GCF [26] the effects of antisymmetrization are not involved into consideration, and for the WF of the relative motion NN-B an "averaged" Gaussian form is assumed.

Previously, the TISM spectroscopic approach was used to analyze the experimental data [34,35] on the quasielastic knock-out of fast deuterons from light nuclei ^{6,7}Li and ^{12}C by protons at 670 MeV. In these (p, pd) processes, the large

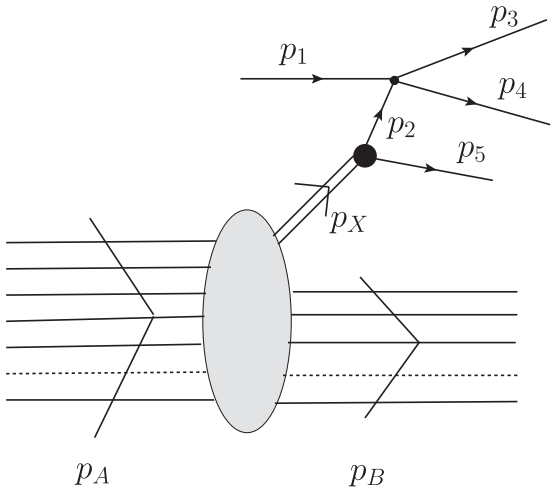

FIG. 1. The amplitude of the process $A(p, ppN)B$. The lines are marked with four-momenta of the particles: the initial (p_A) and final (p_B) nuclei, beam proton (p_1), correlated NN pair (p_X), struck proton (p_2), outgoing fast protons (p_3 and p_4), and outgoing slow nucleon (p_5).

momentum transfer ($\approx$1.6 GeV/c) from the proton beam to the knocked-out deuteron selects the high-momentum component of the internal pn WF associated with compact deuteron configurations. The TISM allows to describe the shapes of the measured spectra when absorptive ISI and FSI are taken into account [36,37].

In Ref. [38], the quasielastic interaction with the dineutron $p\langle nn\rangle \to d + n$ has been experimentally studied in addition to the $p\langle pn\rangle \to d + p$. In Ref. [39], the measured ratio of events $\langle nn\rangle/\langle pn\rangle$ has been reproduced reasonably well assuming the dominance of the Δ-isobar mechanism of the $p\langle nN\rangle \to d + N$ process [40]. The review of these works was done in [37].

The paper is organized as follows. In Sec. II we explain the underlying model starting from the impulse approximation (IA) amplitude. The ISI and FSI are included in the eikonal approximation. Then, in Sec. III we compare our results with the BM@N data [19] and also give predictions for the absolute cross sections. Section IV contains the summary of our results and possible further steps.

II. THE MODEL

The Feynman diagram of the IA amplitude is displayed in Fig. 1. For brevity, we use the notation "X" for the correlated NN pair. The corresponding invariant matrix element is then expressed as follows:

$$M^{\rm IA} = M_{\rm hard}(p_3, p_4, p_1)\frac{i\Gamma_{X\to pN}(p_X, p_5)}{p_2^2 - m^2 + i\epsilon}\frac{i\Gamma_{A\to XB}(p_A, p_B)}{p_X^2 - m_X^2 + i\epsilon}, \tag{2}$$

where $M_{\rm hard}(p_3, p_4, p_1)$ is the amplitude of hard elastic pp scattering, $\Gamma_{A\to XB}(p_A, p_B)$ and $\Gamma_{X\to pN}(p_X, p_5)$ are the decay vertices. Since the nucleus B and nucleon 5 are on the mass shell, the decay vertices can be expressed in terms of the WFs of the relative motion in momentum space and particle energies (see derivation in Ref. [41]):

$$\frac{i\Gamma_{A\to XB}(p_A, p_B)}{p_X^2 - m_X^2 + i\epsilon} = S_A^X\left(\frac{2E_B m_A}{p_X^0}\right)^{1/2}(2\pi)^{3/2}\psi_{n\Lambda}^{M_\Lambda}(-\boldsymbol{p}_X), \tag{3}$$

$$\frac{i\Gamma_{X\to pN}(p_X, p_5)}{p_2^2 - m^2 + i\epsilon} = \left(\frac{2E_5 m_X}{p_2^0}\right)^{1/2}(2\pi)^{3/2}\sqrt{2}\psi_X(\boldsymbol{p}_2), \tag{4}$$

where all quantities on the right-hand side (r.h.s.) are defined in the rest frame (r.f.) of decaying particle, i.e., of the nucleus A in Eq. (3) and of the NN pair in Eq. (4). $\psi_{n\Lambda}^{M_\Lambda}(-\boldsymbol{p}_X)$ is the WF of the relative motion of the NN pair and nucleus B, where n is the number of the oscillator quanta, Λ is the orbital angular momentum, and M_Λ is its z component.[2] $\psi_X(\boldsymbol{p}_2)$ is the internal WF of the NN pair. The factor $\sqrt{2}$ in the r.h.s. of Eq. (4) comes from the antisymmetrized plane wave product WF of the decay nucleons. The normalization conditions of the WFs are

$$\int d^3p\left|\psi_{n\Lambda}^{M_\Lambda}(\boldsymbol{p})\right|^2 = 1, \tag{5}$$

$$\int d^3p|\psi_X(\boldsymbol{p})|^2 = 1, \tag{6}$$

where in the last equation the sum over spin and isospin z components of the decay nucleons is implicitly assumed. In Eq. (3), S_A^X is the spectroscopic amplitude of the transition from a given state of the nucleus A to a given state of the system XB, see Refs. [42,43]:

$$\begin{aligned} S_A^X &= \binom{A}{2}^{1/2}\langle\Psi_A|\Psi_B, n\Lambda, \Psi_X\rangle \\ &= \binom{A}{2}^{1/2}\sum_{\mathcal{L}J_0M_0}\begin{Bmatrix} L_B & S_B & J_B \\ \mathcal{L} & S_X & J_0 \\ L & S & J \end{Bmatrix}\sqrt{(2L+1)(2S+1)(2J_B+1)(2J_0+1)}\,U(\Lambda L_X J_0 S_X; \mathcal{L}J_X) \\ &\times \langle AN_A[f](\lambda\mu)\alpha LST|(A-2)N_B[f_B](\lambda_B\mu_B)\alpha_B L_B S_B T_B; n\Lambda, 2N_X[f_X](\lambda_X\mu_X)\alpha_X L_X S_X T_X\{\mathcal{L}\}\rangle \\ &\times (J_B M_B J_0 M_0|JM)\,(\Lambda M_\Lambda J_X M_X|J_0 M_0)\,(T_B M_{T_B} T_X M_{T_X}|TM_T). \end{aligned} \tag{7}$$

[2]Minus sign in the argument is related to the definition of the WF in the coordinate space, see Eq. (8) below.

Here, the internal WF of the initial nucleus $\Psi_A \equiv |AN_A[f](\lambda\mu)\alpha LSTJMM_T\rangle$ is characterized by the following quantum numbers: N_A—the number of the oscillator quanta, $[f]$—the Young scheme, $(\lambda\mu)$—the Elliott symbol, L, S, J—the orbital, spin, and total angular momenta, respectively, T—isospin, M and M_T—z components of J and T, respectively. α denotes some possible additional quantum numbers needed for complete definition of the state. Similar quantum numbers are also used to characterize the internal WFs of the final nucleus $\Psi_B \equiv |(A-2)N_B[f_B](\lambda_B\mu_B)\alpha_B L_B S_B T_B J_B M_B M_{T_B}\rangle$, and NN correlation $\Psi_X \equiv |2N_X[f_X](\lambda_X\mu_X)\alpha_X L_X S_X T_X J_X M_X M_{T_X}\rangle$. The numbers of oscillator quanta satisfy the oscillator rule, Eq. (1). In Eq. (7), the standard notations for the $6j$ and $9j$ symbols are used, as defined in Ref. [44], while the factor $\langle\cdots\rangle$ is the fractional parentage coefficient (FPC) of the TISM. The FPC enters the decomposition of the internal fully antisymmetric WF of the nucleus A to the products of fully antisymmetric internal WF of the nucleus B, WF of the relative motion of B and NN correlation X, and fully antisymmetric internal wave function of X:

$$
\begin{aligned}
|AN_A[f](\lambda\mu)\alpha LSTM_LM_SM_T\rangle = \sum & (L_BM_{L_B}\mathcal{L}M_{\mathcal{L}}|LM_L)\,(\Lambda M_\Lambda L_X M_{L_X}|\mathcal{L}M_{\mathcal{L}})(S_BM_{S_B}S_XM_{S_X}|SM_S)\,(T_BM_{T_B}T_XM_{T_X}|TM_T) \\
& \times \langle AN_A[f](\lambda\mu)\alpha LST|(A-2)N_B[f_B](\lambda_B\mu_B)\alpha_B L_B S_B T_B; n\Lambda, 2N_X[f_X](\lambda_X\mu_X)\alpha_X L_X S_X T_X\{\mathcal{L}\}\rangle \\
& \times |(A-2)N_B[f_B](\lambda_B\mu_B)\alpha_B L_B S_B T_B M_{L_B} M_{S_B} M_{T_B}\rangle \\
& \times \psi_{n\Lambda}^{M_\Lambda}(\boldsymbol{R}_B - \boldsymbol{R}_X)\,|2N_X[f_X](\lambda_X\mu_X)\alpha_X L_X S_X T_X M_{L_X} M_{S_X} M_{T_X}\rangle, \qquad (8)
\end{aligned}
$$

where the sum is taken over all quantum numbers apart from those entering the WF of the nucleus A. In Eq. (8), the WF of the nucleus B depends on the fixed set of variables $x_1, x_2, \ldots, x_{A-2}$ while the WF of the correlation X depends on the remaining variables x_{A-1} and x_A. Here, $x_i \equiv (\boldsymbol{r}_i, \lambda_i, t_i)$ denote the position $\boldsymbol{r}_i$, spin λ_i, and isospin t_i variable of the ith nucleon. The c.m. coordinates of the nucleus B and correlation X are

$$
\boldsymbol{R}_B = \frac{1}{A-2}\sum_{i=1}^{A-2}\boldsymbol{r}_i \qquad (9)
$$

and

$$
\boldsymbol{R}_X = \tfrac{1}{2}(\boldsymbol{r}_{A-1} + \boldsymbol{r}_A), \qquad (10)
$$

respectively.[3]

As discussed in Sec. I, only the ground state and low-lying excited states of the residual nucleus contribute to the reaction rate. This excludes the excitation of the α core and selects the states of the residual nucleus with the minimum number of oscillator quanta. The FPC of the TISM can be expressed via the FPC of the conventional shell model, and for the considered case the following relationship is used [42]:

$$
\begin{aligned}
&\left\langle AN_A^{\min}[f](\lambda\mu)LST|(A-b)N_B^{\min}[f_B](\lambda_B\mu_B)L_BS_BT_B; n\Lambda, bN_X[f_X](\lambda_X\mu_X)L_XS_XT_X\{\mathcal{L}\}\right\rangle \\
&\quad = (-1)^n\left(\frac{A}{A-b}\right)^{n/2}\binom{A-4}{b}^{1/2}\binom{A}{b}^{-1/2}\langle p^{A-4}[f](\lambda\mu)LST|p^{A-b-4}[f_B](\lambda_B\mu_B)L_BS_BT_B; p^b[f_X](\lambda_X\mu_X)\mathcal{L}S_XT_X\rangle \\
&\qquad \times \langle p^b[f_X](\lambda_X\mu_X)\mathcal{L}S_XT_X|n\Lambda, bN_X[f_X](\lambda_X\mu_X)L_XS_XT_X\rangle, \qquad (11)
\end{aligned}
$$

where b is the number of nucleons in the cluster X. Equation (11) is derived by applying the Bethe-Rose-Elliott-Skyrme theorem [45,46] to the states of the nuclei A and B which are supposed to contain the minimum numbers of the oscillator quanta compatible with Pauli principle. The last factor in the r.h.s. of Eq. (11) is the cluster coefficient, i.e., the overlap integral of the shell model state of b p-wave nucleons with total angular momentum $\mathcal{L}$ and the product of the WF $\psi_{n\Lambda}(\boldsymbol{R}_X)$ and the WF of the TISM $|bN_X[f_X](\lambda_X\mu_X)L_XS_XT_X\rangle$. It is assumed that the last two WFs are vector-coupled and have total angular momentum $\mathcal{L}$.

The expressions (7) and (11) can be easily applied to calculate spectroscopic amplitudes using the two-particle FPCs of the conventional HO shell model given in the tables of Refs. [30,47]. However, before to do this, we need to specify the nuclear states (we use the notation ${}^{(2T+1)(2S+1)}L$ below).

We will apply the shell model with intermediate coupling of Ref. [32] where the TISM basis states have been used to diagonalize the realistic nuclear Hamiltonian that includes—in addition to the HO one-body potential—the Wigner (central), Majorana ($\propto \hat{P}_x$), Bartlett ($\propto \hat{P}_\sigma$) and Heisenberg ($\propto \hat{P}_x\hat{P}_\sigma$)

[3]Since, in Eq. (8), the WF of the nucleus B is the internal one it depends on $(A-3)$ Jacobi coordinates which can be defined as $\boldsymbol{X}_1 = \boldsymbol{r}_1 - \boldsymbol{r}_2$, $\boldsymbol{X}_2 = (\boldsymbol{r}_1 + \boldsymbol{r}_2)/2 - \boldsymbol{r}_3, \ldots, \boldsymbol{X}_i = (\sum_{k=1}^{i}\boldsymbol{r}_k)/i - \boldsymbol{r}_{i+1}, \ldots, \boldsymbol{X}_{A-3} = (\sum_{k=1}^{A-3}\boldsymbol{r}_k)/(A-3) - \boldsymbol{r}_{A-2}$. In a similar way, the internal WF of the correlation X depends only the relative coordinate $\boldsymbol{r}_{A-1} - \boldsymbol{r}_A$.

two-body interactions, and the spin-orbit one-body potential. Contributions of various TISM states to the energy eigenstates of light nuclei obtained in Ref. [32] correspond to the qualitative assessments of Ref. [20]. The intermediate coupling model of Ref. [32] was also used by other authors to calculate the quasielastic knock-out of α particles by protons [48] and electrons [49].

The ^{12}C ground state has quantum numbers $J = T = 0$ and mainly consists of the ^{11}S state with maximum symmetry corresponding to the Young scheme [44]. We neglect small contributions of the [431] ^{13}P and other states. In accordance with Ref. [23] we will also require that the internal WF of the NN SRC does not contain oscillator quanta, i.e., $N_X = 0$ and $L_X = 0$, which corresponds to the choice of the most compact NN configurations. This choice determines the Young scheme $[f_X] = [2]$ and the Elliott symbol $(\lambda_X \mu_X) = (20)$. Furthermore, for the minimum oscillator quantum number $N_B^{min} = 6$ we have $n = 2$ and therefore $\Lambda = 0, 2$. All this allows us to simplify Eq. (7) to the following form:

$$S_A^X = \binom{A}{2}^{1/2} \langle AN_A[f](\lambda\mu)000|(A-2)N_B[f_B](\lambda_B\mu_B)L_BS_BT_B; n\Lambda, 2N_X[f_X](\lambda_X\mu_X)0S_XT_X\{\Lambda\}\rangle$$
$$\times \frac{\delta_{L_B\Lambda}\delta_{S_BS_X}\delta_{S_XJ_X}\delta_{T_BT_X}\delta_{M_{T_B},-M_{T_X}}}{\sqrt{(2L_B+1)(2S_B+1)(2T_B+1)}}(-1)^{J_B-M_B+T_B-M_{T_B}}\,(\Lambda M_\Lambda J_X M_X|J_B,-M_B). \tag{12}$$

Thus, the allowed values are $L_B = \Lambda = 0, 2$. The relevant FPCs are collected in Table I (for a more expanded set of FPCs, see Table 1 of Ref. [43]), and details of their calculation are given in the Appendix. Note that the two-particle orbital FPCs allow coupling of the [44] state of ^{12}C to only [42] or [33] states of the residual nucleus. However, the [33] state of the residual nucleus is coupled with the Young scheme [11] of the NN pair and, thus, can be discarded.

The outgoing nuclei ^{10}B and ^{10}Be can be in excited states. In the present exploratory study, as explained in Sec. I, we will consider only a few low-lying excitations consisting of different TISM states with minimum number of oscillator quanta. The ^{10}B and ^{10}Be states included in our calculations, as well as the partial amplitudes of the contributing TISM states for $A = 10$, are collected in Tables II and III, respectively. The listed levels are confirmed by the compilation of experimental data in Ref. [50]. All of the listed excited states are long-lived and can decay only due to the emission of γ. (The only exception is the ^{10}B $T = 1$, $J = 2$ state with $E^* = 5.17$ MeV that has a photon decay branching ratio of 83% with remaining 17% in the α decay.) The total amplitude for the process ^{12}C$(p, 2pN_s)B$ with the outgoing nucleus B in a certain energy eigenstate is given by a coherent sum

$$M_{\rm tot}^{\rm IA} = \sum_i M_i^{\rm IA}\alpha_i, \tag{13}$$

where $M_i^{\rm IA}$ is the amplitude (2) for the outgoing nucleus B in the TISM eigenstate i, and α_i is the amplitude of the state i in the energy eigenstate, taken from Tables II and III.

ISI and FSI effects can be taken into account by replacing the incoming and outgoing plane waves with distorted waves. In the eikonal approximation, the plane waves of the incoming proton ($i = 1$) and outgoing nucleons ($i = 3, 4, 5$) should be multiplied by absorption factors (c.f. Refs. [51,52])

$$F_i(\boldsymbol{r}) = \exp\left(-\tfrac{1}{2}\sigma_{NN}(p_i)T_i(\boldsymbol{r})\right), \tag{14}$$

where $\sigma_{NN}(p_i)$ is the total NN cross section depending on the momentum of the particle in the r.f. of the nucleus B;

$$T_i(\boldsymbol{r}) = \begin{cases} \int_{-\infty}^{0} d\eta\, \rho(\boldsymbol{r} + \hat{\boldsymbol{p}}_i\eta) & \text{for } i = 1 \\ \int_{0}^{+\infty} d\eta\, \rho(\boldsymbol{r} + \hat{\boldsymbol{p}}_i\eta) & \text{for } i = 3, 4, 5 \end{cases} \tag{15}$$

TABLE I. The FPCs of the TISM $\equiv \langle AN_A^{\rm min}[f](\lambda\mu)LST|(A-b)N_B^{\rm min}[f_B](\lambda_B\mu_B)L_BS_BT_B; n\Lambda, bN_X[f_X](\lambda_X\mu_X)L_XS_XT_X\{\mathcal{L}\}\rangle$ for $A = 12$, $N_A^{\rm min} = 8$, $[f](\lambda\mu) = [44](04)$, $L = S = T = 0$, $N_B^{\rm min} = 6$, $[f_B](\lambda_B\mu_B) = [42](22)$, $b = 2$, $N_X = 0$, $[f_X](\lambda_X\mu_X) = [2](20)$, $L_X = 0$, $S_X = S_B$, $T_X = T_B$.

$^{(2T_B+1)\,(2S_B+1)}L_B$	$n\,\Lambda$	FPC
^{13}S	2 0	$-\sqrt{8/275}$
^{31}S	2 0	$\sqrt{8/275}$
$^{13}D_I$	2 2	$-\sqrt{3/550}$
$^{31}D_I$	2 2	$\sqrt{3/550}$
$^{13}D_{II}$	2 2	$-\sqrt{7/110}$
$^{31}D_{II}$	2 2	$\sqrt{7/110}$

TABLE II. Experimental and theoretical (in parentheses) energy levels of ^{10}B with the partial amplitudes of the TISM states with Young scheme [42]. Taken from Ref. [32].

E^*, MeV	$T\,J$	TISM state	α
0	0 3	$^{13}D_I$	−0.418
		$^{13}D_{II}$	0.679
0.717 (0.68)	0 1	^{13}S	−0.351
		$^{13}D_I$	0.682
		$^{13}D_{II}$	0.541
2.15 (2.08)	0 1	^{13}S	0.885
		$^{13}D_I$	0.307
		$^{13}D_{II}$	0.224
3.58 (3.5)	0 2	$^{13}D_I$	0.401
		$^{13}D_{II}$	0.778
1.74 (1.51)	1 0	^{31}S	0.772
5.17 (5.10)	1 2	$^{31}D_I$	0.728
		$^{31}D_{II}$	0.209

TABLE III. Same as in Table II but for ^{10}Be.

E^*, MeV	$T\,J$	TISM state	α
0	1 0	^{31}S	0.772
3.368 (3.59)	1 2	$^{31}D_I$	0.728
		$^{31}D_{II}$	0.209
5.96 (5.96)	1 2	$^{31}D_I$	−0.226
		$^{31}D_{II}$	0.892

are the thickness functions with $\rho(\boldsymbol{r})$ being the nucleon number density of the nucleus B in the position $\boldsymbol{r}$, and $\hat{\boldsymbol{p}} \equiv \boldsymbol{p}/p$. The absorption-corrected matrix element is obtained by substitution in Eq. (3):

$$(2\pi)^{3/2}\psi^{M_\Lambda}_{n\Lambda}(-\boldsymbol{p}_X) \to \int d^3r e^{-i\boldsymbol{p}_X\boldsymbol{r}}\psi^{M_\Lambda}_{n\Lambda}(-\boldsymbol{r})F_1(\boldsymbol{r})F_3(\boldsymbol{r})F_4(\boldsymbol{r})F_5(\boldsymbol{r}), \quad \boldsymbol{r} = \boldsymbol{R}_X - \boldsymbol{R}_B. \tag{16}$$

To summarize, we can write the following expression for the matrix element, which includes the summation over the magnetic quantum numbers of the intermediate states:

$$M_{\rm tot} = \sum_{\lambda_2} M_{\rm hard}(p_3, p_4, p_1)\left[\left(\frac{2E_5 m_X}{p_2^0}\right)^{1/2} \times (2\pi)^{3/2}\sqrt{2}\sum_{M_X}\psi_X(\boldsymbol{p}_2)\right]_{\rm r.f.of}X \times \sum_i \alpha_i \sum_{M_\Lambda} S^X_{A,i}\left(\frac{2E_B m_A}{p_X^0}\right)^{1/2} \times \int d^3r\, e^{-i\boldsymbol{p}_X\boldsymbol{r}}\psi^{M_\Lambda}_{n_i\Lambda_i}(-\boldsymbol{r})F_{\rm abs}(\boldsymbol{r}), \tag{17}$$

where $F_{\rm abs}(\boldsymbol{r}) \equiv F_1(\boldsymbol{r})F_3(\boldsymbol{r})F_4(\boldsymbol{r})F_5(\boldsymbol{r})$. In Eq. (17), the factor in square brackets is evaluated in the r.f. of NN correlation, and all other factors—in the r.f. of the nucleus A. For simplicity, we will further assume a spin-independent hard amplitude. Note that in the nonrelativistic limit Eq. (17) corresponds to the simplified form of the eikonal approximation [53] used in Ref. [36] for the reaction ^{12}C$(p, pd)\,^{10}$B (except for four absorption factors $F_i(\mathbf{r})$ in Eq. (17) instead of three in Ref. [36]).

Now we can calculate the modulus squared of the matrix element (17):

$$\overline{|M_{\rm tot}|^2} \equiv \frac{1}{2}\sum_{\lambda_1,\lambda_3,\lambda_4,\lambda_5,M_B}|M_{\rm tot}|^2 = \overline{|M_{\rm hard}(p_3, p_4, p_1)|^2}\left(\frac{2E_5 m_X}{p_2^0}\right)(2\pi)^3 2\overline{|\psi_X(\boldsymbol{p}_2)|^2} \times \sum_{i,j}\alpha_i\alpha_j \sum_{M_{\Lambda,i},M_{\Lambda,j}}\sum_{M_B,M_X} S^X_{A,i}S^X_{A,j}\left(\frac{2E_B m_A}{p_X^0}\right) \times \int d^3r \int d^3r' e^{-i\boldsymbol{p}_X(\boldsymbol{r}-\boldsymbol{r}')}\psi^{M_{\Lambda,i}}_{n_i\Lambda_i}(-\boldsymbol{r}) \times \psi^{M_{\Lambda,j}\,*}_{n_j\Lambda_j}(-\boldsymbol{r}')F_{\rm abs}(\boldsymbol{r})F_{\rm abs}(\boldsymbol{r}'), \tag{18}$$

where we neglected the interference of amplitudes with different magnetic quantum numbers M_X of the NN pair and eliminated the spin correlations between $\psi_X(\boldsymbol{p}_2)$ and $M_{\rm hard}(p_3, p_4, p_1)$ by successive replacements

$$\frac{1}{2}\sum_{\lambda_1,\lambda_3,\lambda_4}|M_{\rm hard}(p_3, p_4, p_1)|^2 \to \overline{|M_{\rm hard}(p_3, p_4, p_1)|^2} \equiv \frac{1}{4}\sum_{\lambda_1,\lambda_2,\lambda_3,\lambda_4}|M_{\rm hard}(p_3, p_4, p_1)|^2, \tag{19}$$

$$\sum_{\lambda_2,\lambda_5}|\psi_X(\boldsymbol{p}_2)|^2 \to \overline{|\psi_X(\boldsymbol{p}_2)|^2} \equiv \frac{1}{2J_X+1}\sum_{M_X,\lambda_2,\lambda_5}|\psi_X(\boldsymbol{p}_2)|^2. \tag{20}$$

By using Eq. (12) and the property of the Clebsch-Gordan coefficients

$$\sum_{M_B,M_X}(\Lambda_i M_{\Lambda,i} J_X M_X|J_B, -M_B)(\Lambda_j M_{\Lambda,j} J_X M_X|J_B, -M_B) = \frac{2J_B+1}{2\Lambda_i+1}\delta_{\Lambda_i,\Lambda_j}\delta_{M_{\Lambda,i},M_{\Lambda,j}}, \tag{21}$$

we can simplify Eq. (18) as

$$\overline{|M_{\rm tot}|^2} = (2J_B+1)\overline{|M_{\rm hard}(p_3, p_4, p_1)|^2}\left(\frac{2E_5 m_X}{p_2^0}\right) \times (2\pi)^3 2\overline{|\psi_X(\boldsymbol{p}_2)|^2} \times \sum_{i,j}\alpha_i\alpha_j\delta_{\Lambda_i,\Lambda_j}S^{X0}_{A,i}S^{X0}_{A,j}\left(\frac{2E_B m_A}{p_X^0}\right) \times \int d^3r \int d^3r' e^{-i\boldsymbol{p}_X(\boldsymbol{r}-\boldsymbol{r}')}\frac{1}{2\Lambda_i+1} \times \sum_{M_\Lambda}\psi^{M_\Lambda}_{n_i\Lambda_i}(-\boldsymbol{r})\psi^{M_\Lambda\,*}_{n_i\Lambda_i}(-\boldsymbol{r}')F_{\rm abs}(\boldsymbol{r})F_{\rm abs}(\boldsymbol{r}'), \tag{22}$$

where we introduced the reduced spectroscopic amplitude

$$S^{X0}_{A,i} \equiv \binom{A}{2}^{1/2}\frac{FPC_i}{\sqrt{(2L_B+1)(2S_B+1)(2T_B+1)}} \tag{23}$$

and also used the fact that the value of n_i is fixed for the selected set of FPCs.

It is convenient to perform the double space integration in Eq. (22) in the variables $\boldsymbol{R} \equiv (\boldsymbol{r}+\boldsymbol{r}')/2$, $\boldsymbol{\xi} \equiv \boldsymbol{r}-\boldsymbol{r}'$. In the spirit of the shadowed multiple scattering in Glauber theory [54], the double space integral in Eq. (22) can be then approximately expressed as

$$\int d^3R \int d^3\xi e^{-i\boldsymbol{p}_X\boldsymbol{\xi}}\frac{1}{2\Lambda_i+1}\sum_{M_\Lambda}\psi^{M_\Lambda}_{n_i\Lambda_i}(-\boldsymbol{R}-\boldsymbol{\xi}/2) \times \psi^{M_\Lambda\,*}_{n_i\Lambda_i}(-\boldsymbol{R}+\boldsymbol{\xi}/2)F^2_{\rm abs}(\boldsymbol{R}), \tag{24}$$

where we replaced $\boldsymbol{r}, \boldsymbol{r}' \to \boldsymbol{R}$ in the arguments of the absorption factors $F_{\rm abs}$. This approximation is valid because $F_{\rm abs}(\boldsymbol{r})$ varies with $\boldsymbol{r}$ on a relatively large length scale $2/\rho_0\sigma_{NN} \simeq 3$ fm, where $\rho_0 \simeq 0.16$ fm^{-3} is the nuclear saturation density,

and $\sigma_{NN} \simeq 40$ mb is the NN cross section.[4] In contrast, the WF of the relative $X - B$ motion varies on a shorter length scale of the HO parameter $r_0 \simeq 1.6$ fm (c.f. Ref. [55]) and, moreover, may contain nodes and/or nonmonotonic behavior as a function of R. Thus, we keep the exact arguments in the WFs of Eq. (24), allowing it to be rewritten as

$$\int d^3R f_{n_i\Lambda_i}(-\boldsymbol{R}, -\boldsymbol{p}_X) F^2_{\rm abs}(\boldsymbol{R}), \tag{25}$$

where

$$f_{n_i\Lambda_i}(-\boldsymbol{R}, -\boldsymbol{p}_X) \equiv \int d^3\xi e^{-i\boldsymbol{p}_X\boldsymbol{\xi}} \frac{1}{2\Lambda_i+1} \sum_{M_\Lambda} \psi^{M_\Lambda}_{n_i\Lambda_i}(-\boldsymbol{R}-\boldsymbol{\xi}/2) \times \psi^{M_\Lambda *}_{n_i\Lambda_i}(-\boldsymbol{R}+\boldsymbol{\xi}/2) \tag{26}$$

is a Wigner function which has a meaning of the probability density in the phase space $(\boldsymbol{R}, \boldsymbol{p}_X)$, where $\boldsymbol{R} = \boldsymbol{R}_X - \boldsymbol{R}_B$ is the relative position and $\boldsymbol{p}_X = -\boldsymbol{p}_B$ is the canonically conjugated momentum. The Wigner function satisfies the relations

$$\int \frac{d^3R}{(2\pi)^3} f_{n_i\Lambda_i}(-\boldsymbol{R}, -\boldsymbol{p}_X) = \overline{|\psi_{n_i\Lambda_i}(-\boldsymbol{p}_X)|^2},$$
$$\int \frac{d^3p_X}{(2\pi)^3} f_{n_i\Lambda_i}(-\boldsymbol{R}, -\boldsymbol{p}_X) = \overline{|\psi_{n_i\Lambda_i}(-\boldsymbol{R})|^2}, \tag{27}$$

where the overline means averaging over M_Λ.

As a result, we arrive at the following formula for the modulus squared of the matrix element:

$$\overline{|M_{\rm tot}|^2} = (2J_B+1)\overline{|M_{\rm hard}(p_3, p_4, p_1)|^2} \left(\frac{2E_5 m_X}{p_2^0}\right) \times (2\pi)^3 2\overline{|\psi_X(\boldsymbol{p}_2)|^2} \times \sum_{i,j} \alpha_i\alpha_j\delta_{\Lambda_i,\Lambda_j} S^{X0}_{A,i} S^{X0}_{A,j} \left(\frac{2E_B m_A}{p_X^0}\right) \times \int d^3R\, f_{n_i\Lambda_i}(-\boldsymbol{R}, -\boldsymbol{p}_X) F^2_{\rm abs}(\boldsymbol{R}), \tag{28}$$

where the square of the absorption factor is

$$F^2_{\rm abs}(\boldsymbol{R}) = \exp[-\sigma_{NN}(p_1)T_1(\boldsymbol{R}) - \sigma_{NN}(p_3)T_3(\boldsymbol{R}) - \sigma_{NN}(p_4)T_4(\boldsymbol{R}) - \sigma_{NN}(p_5)T_5(\boldsymbol{R})]. \tag{29}$$

Thus, the way the absorption enters into Eq. (28) has a simple and clear meaning: the partial reaction rate in the IA for the c.m. of the NN correlation located in the space element d^3R relative to the center of the residual nucleus B is multiplied by the probability that the incoming proton will reach the point $\boldsymbol{R}$ without being absorbed,i.e., does not participate in any elastic or inelastic scattering processes, and the outgoing nucleons will reach free space from the point $\boldsymbol{R}$ without being absorbed. We have checked that for the cross sections integrated over momentum of the residual nucleus the approximate formula of Eq. (28) agrees with Eq. (18) with accuracy of ≈20%. This is acceptable for our purposes in this work given the fact that the cross section is reduced by absorption effects by an order of magnitude.

The formula (28) can be simply modified to estimate the contribution of charge exchange (CEX) processes. Since the probability of collision with pp correlation is small, we will take into account only two dominant contributions: (i) when the incoming proton (1) interacts with the proton of pn correlation, and the slow recoil neutron (5) then experiences CEX on a proton from the nucleus B, and (ii) when the incoming proton interacts with the neutron of the pn correlation, and the fast knocked-out neutron (4) then experiences CEX.[5] In the semiclassical approximation, the corresponding CEX probabilities are determined by the following expressions:

$$P_{n_5\to p_5} = F^2_{\rm abs}(\boldsymbol{R})\sigma_{\rm CEX}(p_5)T_5(\boldsymbol{R})/2, \tag{30}$$
$$P_{n_4\to p_4} = F^2_{\rm abs}(\boldsymbol{R})\sigma_{\rm CEX}(p_4)T_4(\boldsymbol{R})/2, \tag{31}$$

where $1/2$ factors are included to obtain proton thickness functions. The total CEX probability is

$$P_{n_5\to p_5} + P_{n_4\to p_4} = F^2_{\rm abs}(\boldsymbol{R})[\sigma_{\rm CEX}(p_5)T_5(\boldsymbol{R}) + \sigma_{\rm CEX}(p_4)T_4(\boldsymbol{R})]/2. \tag{32}$$

Similar expressions for CEX probabilities are used in GCF calculations, see Ref. [56]. To obtain the total reaction rate with outgoing slow proton we sum up the reaction rate of Eq. (28) for the pp correlation and the reaction rate of Eq. (28) for the pn correlation with CEX,i.e., with $F^2_{\rm abs}(\boldsymbol{R})$ replaced by $P_{n_5\to p_5} + P_{n_4\to p_4}$. The back reactions $p \to n$ and the double CEX processes are neglected.

A. Wave functions

So far we have assumed that all WFs of our model are the TISM WFs. However, phenomenology favors the deuteron-like WFs of isoscalar SRCs. Thus, for isoscalar pn pairs we use the deuteron WF of the CD-Bonn model, Ref. [57], which gives

$$\overline{|\psi_{X,T=0}(\boldsymbol{p}_2)|^2} = \frac{1}{2}\frac{u^2(p_2) + w^2(p_2)}{4\pi}. \tag{33}$$

Here, $u(p_2)$ and $w(p_2)$ are, respectively, the S- and D-wave components satisfying the normalization condition

$$\int dp\, p^2[u^2(p) + w^2(p)] = 1. \tag{34}$$

The factor $1/2$ in Eq. (33) comes from the square of the isospin WF. For the free $^1S_0$ pp ($T_z = 1$) and pn ($T_z = 0$) pairs with $T = 1$, the bound state is absent but there is a virtual level (the pole of the S matrix) in the nonphysical region of the relative energy E at $E \approx -0.45$MeV. Thus, for isovector NN pairs we rely on the following formula:

$$\overline{|\psi_{X,T=1}(\boldsymbol{p}_2)|^2} = \tfrac{1}{2}(1+T_z)|\psi_s(p_2)|^2. \tag{35}$$

[4]Due to absorption factors, the integral in Eq. (22) is dominated by a peripheral nuclear region where the nucleon density is smaller than ρ_0. Thus, the actual length scale may even be larger.

[5]In the second case, we assume that $\overline{|M_{\rm hard}|^2}$ is isospin-independent and both the third and fourth nucleons can be neutrons with probability $1/2$, but the probability of CEX is the same for each of them.

Here, $\psi_s(p)$ is the zero-energy solution of $NN(^1S_0)$ scattering problem, Ref. [43],

$$\psi_s(p) = \kappa \frac{f(p,0;0)}{\alpha^2 + p^2}, \tag{36}$$

where $\alpha = 0.104$ fm^{-1} corresponds to a virtual level "binding energy" $-E = \alpha^2/m = 0.45$ MeV, Ref. [58]. $f(p,k;k)$ is the half-off-shell NN scattering amplitude in the $^1S_0$ channel parametrized in Ref. [59]. The factor κ is chosen from the normalization condition

$$4\pi \int dp\, p^2 |\psi_s(p)|^2 = 1. \tag{37}$$

The squared WFs of the relative motion NN-B for the oscillator quantum number $n = 2$ are given by standard expressions from TISM

$$|\psi_{20}(R)|^2 = \frac{3}{2R_0^3\pi^{3/2}}\left[1 - \frac{2}{3}\left(\frac{R}{R_0}\right)^2\right]^2 \exp[-(R/R_0)^2], \tag{38}$$

$$\overline{|\psi_{22}(R)|^2} = \frac{4}{15R_0^3\pi^{3/2}}\left(\frac{R}{R_0}\right)^4 \exp[-(R/R_0)^2], \tag{39}$$

where $R_0 = r_0\sqrt{A/2(A-2)}$ is the HO parameter of the NN-B relative motion, and $r_0 = 1.736$ fm is the conventional HO model parameter fit to describe the momentum distributions of the p-shell and s-shell nucleons in the ^{12}C$(e,e'p)^{11}$B reaction [60].[6] We have also performed calculations using the phenomenological TISM WF of the lowest HO state $n = 0$, $\Lambda = 0$:

$$|\psi_{00}(R)|^2 = \frac{1}{R_0^3\pi^{3/2}} \exp[-(R/R_0)^2], \tag{40}$$

where $R_0 = \sqrt{\alpha_{\rm c.m.}} = 1$ fm [61]. This corresponds to the standard deviation of the relative NN-B momentum distribution $\sigma_{\rm c.m.} = 1/\sqrt{2\alpha_{\rm c.m.}} = 139.5\,\text{MeV}/c$, which is consistent with $\sigma_{\rm c.m.} = (156 \pm 27)\,\text{MeV}/c$ obtained from analysis of BM@N data [19].

According to the oscillator rule, Eq. (1), WFs with $n = 2$ correspond to transitions into s^4p^6 configurations, and $n = 0$—into s^2p^8 configurations of the residual nucleus. Since the latter configurations, most likely, are not included into the BM@N data in question, taking $n = 0$ is not allowed by the oscillator rule. However, we consider here this option too for comparison with other SRC models where this option is often used.

The normalization of the NN-B WFs is such that

$$4\pi \int dR\, R^2\, \overline{|\psi_{n\Lambda}(R)|^2} = 1. \tag{41}$$

The transition to the WFs in momentum space is simply reached by replacing $R \to p_X$ and $R_0 \to 1/R_0$ in Eqs. (38), (39) and (40).

[6]The conventional shell model fit to the differential cross section of elastic p ^{12}C scattering at 1 GeV gives $r_0 = 1.581$ fm [55] which does not lead to significant changes in our numerical results.

For the calculations with absorption, we need to specify the Wigner functions, Eq. (26). After somewhat lengthy but straightforward calculations we arrive at the following formulas:

$$f_{20}(-\boldsymbol{R}, -\boldsymbol{p}_X) = 8\, e^{-(R^2 + p_X^2 R_0^4)/R_0^2}\Big[\frac{2}{3R_0^4}\big(R^4 + p_X^4 R_0^8\big) - \frac{4}{3}R^2 p_X^2 + 1 - \frac{4}{3R_0^2}\big(R^2 + p_X^2 R_0^4\big) + \frac{8}{3}(\boldsymbol{R}\boldsymbol{p}_X)^2\Big], \tag{42}$$

$$f_{22}(-\boldsymbol{R}, -\boldsymbol{p}_X) = 8\, e^{-(R^2 + p_X^2 R_0^4)/R_0^2}\Big[\frac{4}{15R_0^4}\big(R^4 + p_X^4 R_0^8\big) + \frac{16}{15}R^2 p_X^2 + 1 - \frac{4}{3R_0^2}\big(R^2 + p_X^2 R_0^4\big) - \frac{8}{15}(\boldsymbol{R}\boldsymbol{p}_X)^2\Big], \tag{43}$$

$$f_{00}(-\boldsymbol{R}, -\boldsymbol{p}_X) = 8\, e^{-(R^2 + p_X^2 R_0^4)/R_0^2}. \tag{44}$$

B. Elementary cross sections

Experimental data on pp elastic large-angle differential cross section $d\sigma/d\Omega_{\rm c.m.}$ at $p_{\rm lab} = 4\,\text{GeV}/c$ are reported in Ref. [62] as a function of the c.m. polar scattering angle $\Theta_{\rm c.m.}$. To get the square of the hard scattering amplitude, we used a simple relation

$$\overline{|M_{\rm hard}(p_3, p_4, p_1)|^2} = 64\pi^2 s\, d\sigma/d\Omega_{\rm c.m.}, \tag{45}$$

where $\Theta_{\rm c.m.} = \arccos[1 + \max(t,u)/2(s/4 - m^2)]$, $s = (p_3 + p_4)^2$, $t = (p_1 - p_3)^2$, $u = (p_1 - p_4)^2$.

The experimental total pp and pn cross sections at the beam momentum $p < 5\,\text{GeV}/c$ are well described by the parametrization of Ref. [63] which we use in calculation of the absorption factor (29) with appropriate weighting according to the proton and neutron numbers so that the pN and nN cross sections are

$$\sigma_{pN} = [\sigma_{pp}Z_B + \sigma_{pn}(A_B - Z_B)]/A_B, \tag{46}$$

$$\sigma_{nN} = [\sigma_{pn}Z_B + \sigma_{pp}(A_B - Z_B)]/A_B, \tag{47}$$

where Z_B and A_B are, respectively, the charge and mass numbers of the residual nucleus B.

The CEX cross section $np \to pn$ is defined as the integrated elastic np differential cross section at large $\Theta_{\rm c.m.}$, typically at $\Theta_{\rm c.m.} > 90^\circ$. Experimental data of Ref. [64] at $E = 800$ MeV give $\sigma_{\rm CEX}(800) = 4.25$ mb for $\Theta_{\rm c.m.} = 135^\circ$–$180^\circ$. The CEX cross section at other energies can be determined from the scaling relation valid for $p_{\rm lab} < 100\,\text{GeV}/c$, established in Ref. [65]:

$$\sigma_{\rm CEX}(E) = \sigma_{\rm CEX}(800)\frac{s(800)}{s(E)}, \tag{48}$$

where $s(E) = 2m(E + 2m)$.

C. Observables

The full differential cross section of the reaction $A(p, 2pN_s)B$ is given by the standard formula (see Fig. 1 for particle notation)

$$d\sigma_{1A\to 345B} = \frac{(2\pi)^4 \overline{|M_{\rm tot}|^2}}{4I} d\Phi_4, \tag{49}$$

where $I = [(p_1 p_A)^2 - m^2 m_A^2]^{1/2}$ is the flux factor and

$$d\Phi_4 = \delta^{(4)}(p_1 + p_A - p_3 - p_4 - p_5 - p_B) \times \frac{d^3p_3}{(2\pi)^3 2E_3} \frac{d^3p_4}{(2\pi)^3 2E_4} \frac{d^3p_5}{(2\pi)^3 2E_5} \frac{d^3p_B}{(2\pi)^3 2E_B} \tag{50}$$

is the four-body invariant phase space. In order to perform comparison with the BM@N data [19], we have to integrate Eq. (49) over full four-body phase space applying experimental cuts. It is convenient to perform this in the following way. First, we separate the two-body phase space $d\Phi_2$ of the outgoing fast protons:

$$d\Phi_2 = \delta^{(4)}(\mathcal{P} - p_3 - p_4) \frac{d^3p_3}{(2\pi)^3 2E_3} \frac{d^3p_4}{(2\pi)^3 2E_4}, \tag{51}$$

where $\mathcal{P} = p_1 + p_A - p_5 - p_B$. Integrating Eq. (51) over d^3p_4 and dp_3 gives the following result:

$$d\Phi_2 = \frac{p_3 d\Omega_3}{(2\pi)^6 4|E_3 + E_4 - E_3 \mathcal{P}\chi/p_3|}, \tag{52}$$

where $d\Omega_3$ is the solid angle of the third proton and $\chi \equiv \boldsymbol{\mathcal{P}}\boldsymbol{p}_3/\mathcal{P}p_3$. All quantities in Eq. (52) are defined in the laboratory frame, i.e., in the r.f. of the first proton. The momentum of the third proton is found by solving the equation $E_3 + E_4 = \mathcal{P}^0$, which gives two solutions:

$$p_3 = \frac{M^2 \mathcal{P}\chi \pm \mathcal{P}^0 \sqrt{M^4 - 4m^2[(\mathcal{P}^0)^2 - \boldsymbol{\mathcal{P}}^2\chi^2]}}{2[(\mathcal{P}^0)^2 - \boldsymbol{\mathcal{P}}^2\chi^2]} \tag{53}$$

with $M = \sqrt{\mathcal{P}^2}$ being the invariant mass of the third and fourth protons. [In the case where both values of p_3 pass the BM@N acceptance, the r.h.s. of Eq. (52) is summed over these two values.]

The integrations of Eq. (50) over three-momenta of the fifth nucleon and residual nucleus should be performed in the r.f. of ^{12}C since the internal WF of the NN correlation and the WF of relative NN-B motion favor small momenta in that frame. Replacing integration over d^3p_5 by integration over d^3p_2 (which is more convenient since the BM@N acceptance restricts $|\boldsymbol{p}_2|$) we come to the following formula for the integrated cross section:

$$\sigma_{1A\to 345B} = \frac{1}{64(2\pi)^8 p_{\rm beam} m} \int d\Omega_3 \int d^3p_2 \times \int \frac{d^3p_B}{E_5 E_B} \frac{\overline{|M_{\rm tot}|^2} p_3}{|E_3 + E_4 - E_3 \mathcal{P}\chi/p_3|}, \tag{54}$$

where the energies E_5 and E_B are defined in the r.f. of ^{12}C, and $p_{\rm beam}$ is the momentum of ^{12}C in the laboratory frame. The single differential cross sections $d\sigma/dx$ where x is any kinematic observable are obtained by multiplying the integrand of Eq. (54) by $\delta(x - x(\Omega_3, \boldsymbol{p}_2, \boldsymbol{p}_B))$.

Let us now summarize the BM@N acceptance cuts which are included when taking the integrals in Eq. (54):

(i) Velocities of fast protons in the laboratory frame: $0.8 < \beta_{3,4} < 0.96$.
(ii) Polar angles of fast protons in the laboratory frame: $24^\circ < \Theta_{3,4} < 37^\circ$.
(iii) Azimuthal angles of fast protons in the laboratory frame: $-14^\circ < \phi_3 < 14^\circ$, $-180^\circ < \phi_4 < -166^\circ$, and $166^\circ < \phi_4 < 180^\circ$.
(iv) In-plane opening angle: $\Theta_3 + \Theta_4 > 63^\circ$.
(v) Missing momentum in the r.f. of ^{12}C: $0.350\,{\rm GeV}/c < p_2 < 1.2\,{\rm GeV}/c$.
(vi) Missing energy $E_{\rm miss} \equiv m - p_2^0$ in the r.f. of ^{12}C: $-0.110\,{\rm GeV} < E_{\rm miss} < 0.240\,{\rm GeV}$.

The calculation of the integrated cross section, Eq. (54), includes the eight-dimensional integral over phase space. In this case, if absorption is included in the modulus squared of the matrix element, the integral becomes 11-dimensional[7] which makes the direct numerical calculation impossible. In order to overcome this problem, we have tabulated the absorption integral, Eq. (25), as a function of the momentum of slow nucleon, $\boldsymbol{p}_5$. The $\boldsymbol{p}_X$ dependence has been factorized out by using explicit forms, Eqs. (42)–(44), of Wigner functions. The momenta of fast protons have been fixed by the condition of free pp scattering at $\Theta_{\rm c.m.} = 90^\circ$ which approximately corresponds to the middle of the experimental acceptance region. By selecting different kinematics within detector acceptance we have checked that this approximation works very well.

III. RESULTS

In this section we present the results of our calculations of various single differential cross sections of the reaction channel $^{12}{\rm C}(p, 2pn_s)\,^{10}{\rm B}$ compared to BM@N data from Ref. [19]. Data points are scaled by conveniently chosen factors to facilitate comparison of measured distribution shapes with calculated ones.

Figure 2 shows the distributions of the invariants $t = (p_1 - p_3)^2$ and $u = (p_1 - p_4)^2$. The distributions are governed by hard $pp \to pp$ scattering and are sensitive neither to the relative WFs of the NN-B motion nor to the absorption. [Note that the insensitivity to the absorption might be partly related to the fixed kinematics of fast protons in the calculation of the absorption integral, Eq. (25), as discussed in the end of Sec. II. More precise calculation may change this result but is beyond the scope of our present exploratory study.] The calculation predicts maxima at $|t| = |u| \simeq 1.5\,{\rm GeV}^2$, which are not in the data. This discrepancy might be, however, attributed to large experimental bins and statistical errors.[8]

[7]The thickness functions, Eq. (15), have been calculated analytically by using the HO density profile of the residual nucleus $\rho(r) = \frac{4}{r_0^3\pi^{3/2}}[1 + \frac{A_B-4}{6}(\frac{r}{r_0})^2]e^{-r^2/r_0^2}$.

[8]The calculated $|t|$ and $|u|$ distributions are identical within numerical integration errors ($\approx$10%) which is expected due to the reflection symmetry of experimental setup with respect to the yz

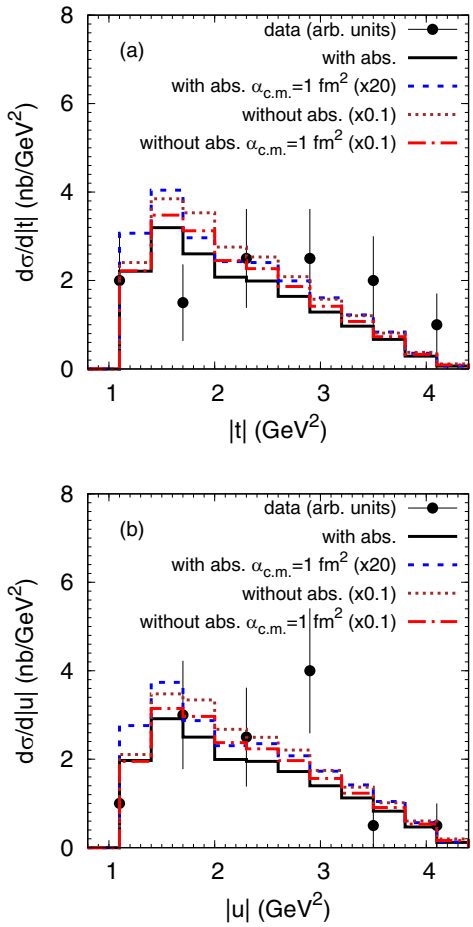

FIG. 2. Distributions of (a) $|t|$ and (b) $|u|$ in the process ^{12}C$(p, 2pn_s)\,^{10}$B. Calculations using the TISM WF of relative NN-B motion Eqs. (38), (39) with and without absorption are shown by the solid (black) and dotted (brown) lines, respectively. Calculations using the lowest HO state WF Eq. (40) with and without absorption are shown by the dashed (blue) and dot-dashed (red) lines, respectively. The calculated results are scaled by factors shown in parentheses. Experimental data are from Ref. [19].

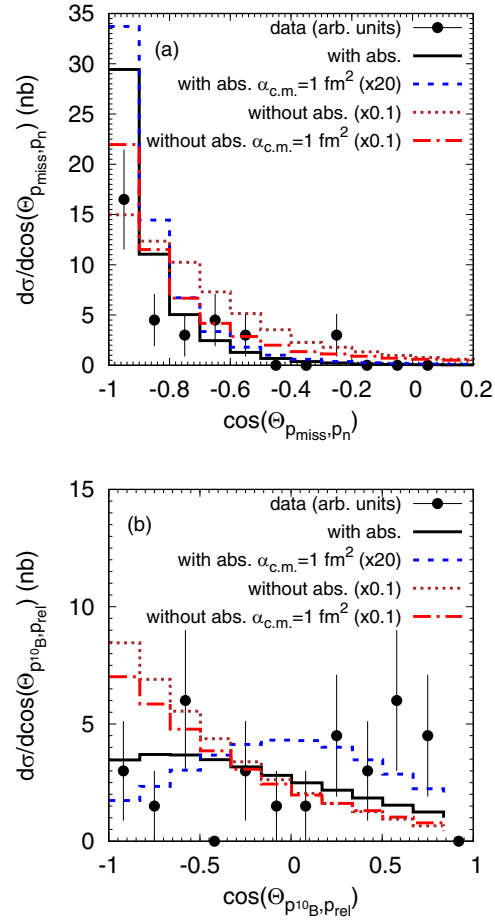

FIG. 3. Distributions of cosine of angle between missing momentum and neutron momentum (a) and between ^{10}B momentum and relative momentum $\boldsymbol{p}_{\rm rel} \equiv (\boldsymbol{p}_2 - \boldsymbol{p}_5)/2$ (b). Notations are the same as in Fig. 2.

The distribution of the cosine of angle between $\boldsymbol{p}_{\rm miss} \equiv \boldsymbol{p}_2$ and $\boldsymbol{p}_n \equiv \boldsymbol{p}_5$ in the r.f. of the target nucleus is shown in Fig. 3(a). Without absorption, the phenomenological WF gives a narrower relative NN-B momentum distribution and, therefore, results in a sharper back-to-back correlation between missing momentum and neutron momentum. Including absorption leads to a somewhat more sharp back-to-back correlation. Similar effect of FSIs was also obtained in the calculations of Ref. [23] for the opening angle distribution of the initial-state protons in the $A(e, e'pp)$ reactions.

Figure 3(b) displays the distribution of the cosine of the angle between the momentum of the outgoing nucleus and the relative momentum of nucleons in the NN pair. The calculations without absorption produce dropping cross sections with decreasing angle and are only weakly sensitive to the WFs of relative NN-B motion. Including absorption strongly reduces the yield at 180° due to enhanced absorption of low-energy neutrons. The phenomenological WF places the NN pair, on average, closer to the center of the residual nucleus that leads to stronger absorption as compared to the TISM WFs. As a result, the angle distributions calculated with absorption are sensitive to the WFs. Note that our calculation with phenomenological WF with absorption gives a weak maximum at 90°, in-line with the GCF result (see Fig. 4(e) in Ref. [19]). The BM@N data points seem to indicate no angle dependence.

As is well known, nucleons with high momentum bound in stable nuclei are strongly off mass shell. This is seen from the distribution of missing energy shown in Fig. 4. Indeed, according to the two-nucleon correlation model [66], neglecting c.m. motion of the NN pair, the energy of the struck proton can be estimated as

$$p_2^0 = 2m - B_A + B_{A-2} - \sqrt{\boldsymbol{p}_2^2 + m^2}, \qquad (55)$$

where B_A and B_{A-2} are the binding energies of the initial (^{12}C) and final (^{10}B) nuclei, respectively. This gives the missing

plane. However, the measured $|t|$ and $|u|$ distributions differ from each other.

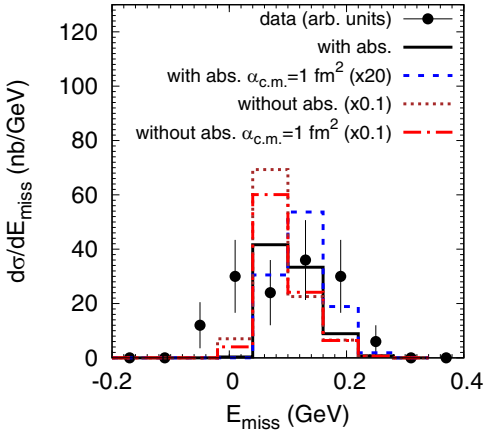

FIG. 4. Distribution of missing energy. Notations are the same as in Fig. 2.

energy

$$E_{\rm miss} = m - p_2^0 = B_A - B_{A-2} - m + \sqrt{\boldsymbol{p}_2^2 + m^2}. \qquad (56)$$

Substituting values $B_A = 7.68 \times 12\,\text{MeV}$, $B_{A-2} = 6.48 \times 10\,\text{MeV}$ [67], and $|\boldsymbol{p}_2| = 350$–$500\,\text{MeV}/c$ one gets from Eq. (56) $E_{\rm miss} = 90$–$152\,\text{MeV}$ in qualitative agreement with the experimental $E_{\rm miss}$ distribution. Our numerical results correctly reproduce the centroid position of the measured $E_{\rm miss}$ distribution, but underestimate the width. Note that our calculations give a better agreement with experimental $E_{\rm miss}$ distributions when absorption is included. This can be again explained by stronger absorption of slow recoil neutron which corresponds to smaller $E_{\rm miss}$ values.

Figures 5(a), 5(b), and 5(c) show, respectively, the distributions over the x, y, and z components of the missing momentum. Our calculations describe the data quite well irrespective of the presence of absorption and the choice of the WFs.[9] The same is true for the $p_{\rm miss}$ distribution shown in Fig. 5(d).

Figures 5(e), 5(f), and 5(g) show, respectively, the distributions over the x, y, and z components of the momentum of the outgoing ^{10}B. It is expected that these distributions should be most sensitive to the WF of relative NN-B motion. Indeed, for calculations without absorption, the TISM WFs give broader distributions as compared to those of the phenomenological WF. Including absorption does not change this conclusion.

Figure 5(h) shows the momentum distribution of ^{10}B. Absorption noticeably influences the spectra at large values of

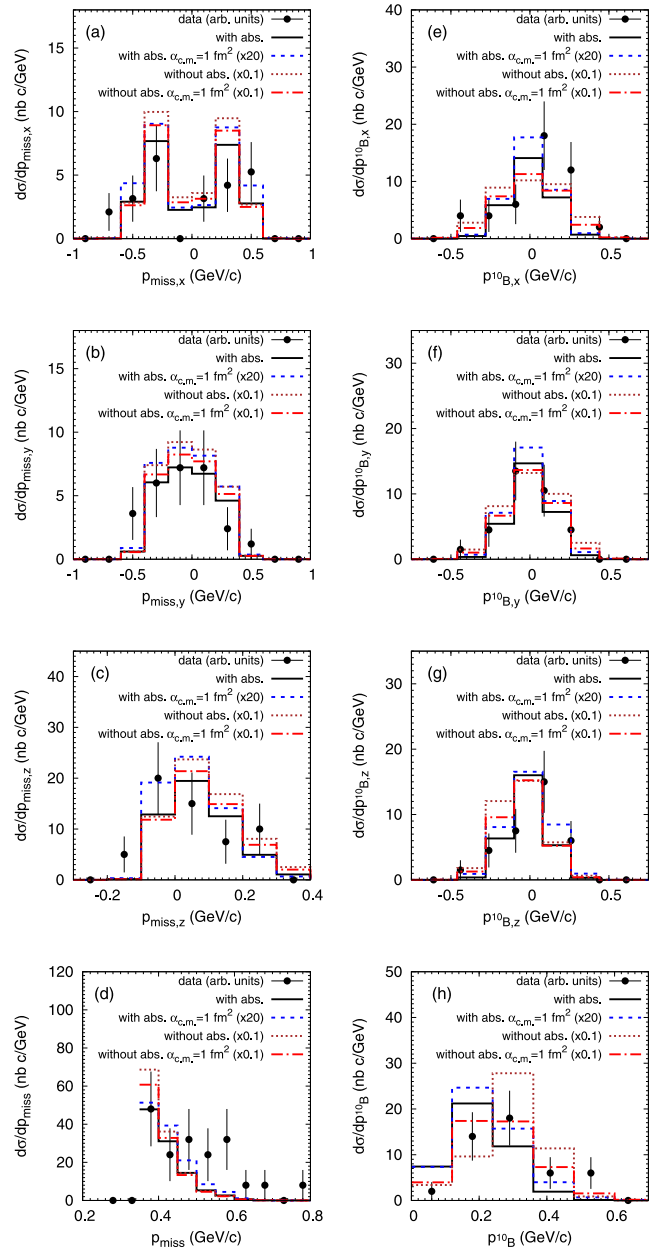

FIG. 5. Distributions of missing momentum (a), (b), (c), and (d) and of the residual nucleus momentum (e), (f), (g), and (h). Notations are the same as in Fig. 2.

$p_{^{10}B}$. This is explained by the $p_{\rm miss} > 350\,\text{MeV}/c$ cut. As a consequence of momentum conservation in the ^{12}C rest frame ($\boldsymbol{p}_{\rm miss} + \boldsymbol{p}_n + \boldsymbol{p}_{^{10}B} = 0$), at small $p_{^{10}B}$, this cut selects kinematics with neutrons of larger momenta which experience less absorption, while at large $p_{^{10}B}$, kinematics with neutrons of smaller momenta, which are suppressed by a stronger absorption, is accepted too.

Since the TISM calculation directly includes transitions to different internal states of the residual nucleus, it is instructive to examine partial contributions of various transitions. Figure 6 shows the excitation energy spectrum of ^{10}B. The partial contributions of the $T = 0$ states are also shown. ($T = 1$ states are included in the total spectrum but not shown since their

[9]The calculated $p_{{\rm miss},z}$ distributions are shifted towards positive $p_{{\rm miss},z}$ values. However, in calculations we applied the $pp \to pp$ differential cross section parametrization at fixed $\sqrt{s}$ (see Sec. II B). This does not allow us to explain the shift by the s^{-10} scaling of the pp hard elastic cross section at fixed $\Theta_{\rm c.m.}$ [68,69]. The shift is rather caused by the specific angular acceptance of the two-arm spectrometer [19] configured for pp scattering at $\Theta_{\rm c.m.} = 90^\circ$ for $p_{\rm lab} = 4\,\text{GeV}/c$. Larger $p_{\rm lab}$ corresponding to negative $p_{{\rm miss},z}$ would decrease the polar scattering angle in the laboratory frame beyond the detector acceptance.

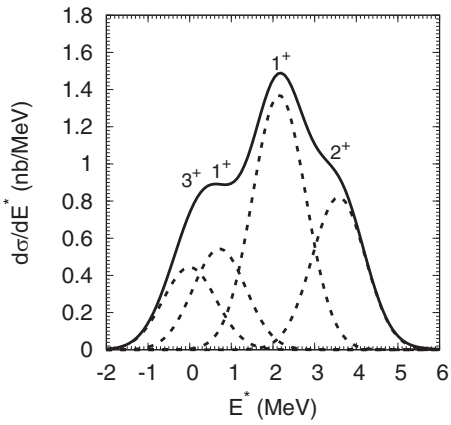

FIG. 6. Distribution of the residual nucleus ^{10}B excitation energy (solid line) obtained by summing the partial cross sections for different energy eigenstates folded for illustration purpose with the Gaussian distributions of the typical experimental resolution FWHM = 1.5 MeV (dashed lines).

contribution is very small.) The spectrum is dominated by the 2.15 MeV 1^+ state that has 95% contribution of the S wave. The 0.717 MeV 1^+ state has 38% contribution of the S wave. The 3^+ ground state and the 3.58 MeV 2^+ state are pure D-wave ones. Thus, selecting different windows of the excitation energy it is possible to restrict the partial waves in the relative NN-B WF. Note that the dominant production of the residual nucleus in the excited (and not ground) state was also found in the calculations of the ^{12}C$(p, pd)\,^{10}$B process in Ref. [31]. As we see from Table I, the orbital angular momentum of the residual nucleus dictates the angular momentum of the relative NN-B WF and, thus, the residual nucleus momentum distribution and the absorptive effect of ISI/FSI. In Fig. 7, we examine the momentum distributions of the residual ^{10}B nuclei in the S- and D-wave states. The D-wave component has a harder momentum spectrum and seems to agree with data better. Thus, the present BM@N data may indicate an

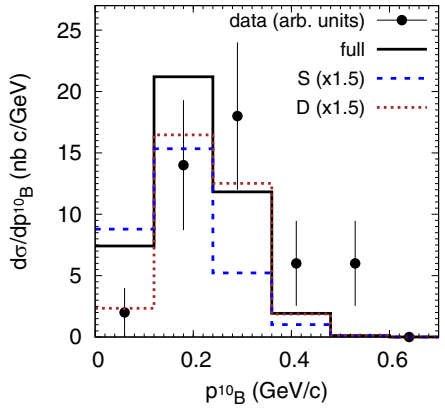

FIG. 7. Distribution of the residual nucleus ^{10}B momentum. Solid (black) line—full calculation with TISM WFs including absorption. Dashed and dotted lines show, respectively, the partial contributions of transitions to the S and D states of ^{10}B scaled by a factor of 1.5. Experimental data are from Ref. [19].

TABLE IV. Integrated cross sections (in nb) in the kinematics of the BM@N experiment [19]. Lower line gives the ratio $R = \sigma[^{12}\mathrm{C}(p, 2pp_s)\,^{10}\mathrm{Be}]/\sigma[^{12}\mathrm{C}(p, 2pn_s)\,^{10}\mathrm{B}]$ (in %). Results obtained with phenomenological relative NN-B WFs [see Eq. (40)] are given in parentheses.

	IA	Abs	Abs+CEX
^{12}C$(p, 2pn_s)^{10}$B	63.7 (57.1)	5.1 (0.31)	5.0 (0.29)
^{12}C$(p, 2pp_s)^{10}$Be	4.2 (3.3)	0.13 (0.0058)	0.23 (0.030)
R	6.6 (5.8)	2.5 (1.8)	4.6 (10.4)

enhanced contribution of the D wave as compared to the amplitudes of Table II.

We will finally discuss the isospin composition of SRCs. Table IV lists our results for the integrated cross sections of the two-nucleon knock-out with outgoing ^{10}B and ^{10}Be and their ratio R. The latter has to be compared with experimental value $R = 2/23 = (8.7 \pm 6)\%$. (The total numbers of detected events with ^{10}Be and ^{10}B are 2 and 23, respectively, as reported in Ref. [19]. The included statistical error is our estimation.)

In the IA, the results are not much sensitive to the different WFs of relative NN-B motion. Including absorption reduces cross section by an order of magnitude in the case of the TISM WFs and by more than two orders—in the case of phenomenological WFs. Especially strong absorption effect is visible for the channel with ^{10}Be for phenomenological WFs. This is because, on one hand, the $n = 0$, $\Lambda = 0$ WF is peaked at $p_B = 0$, but in this case the yield is very strongly suppressed by the $^1S_0$ NN relative WF at $p_{\mathrm{miss}} > 350\,\mathrm{MeV}/c$. On other hand, at finite p_B, the yield is suppressed by strong absorption of low-momentum neutrons.

Including CEX increases the cross section of the ^{10}Be channel by about 50% for TISM WFs and five times for phenomenological WFs. Thus, in the latter case, almost all ^{10}Be yield is due to the CEX processes. The stronger absorption and CEX for phenomenological WFs arise from smaller average relative NN-B distances, which force participating nucleons to travel through a region of higher density of the residual nucleus. Phenomenological WFs provide the best agreement with experiment for the ratio R.

IV. SUMMARY

We applied the TISM to the hard proton knock-out reactions ^{12}C$(p, 2pn_s)\,^{10}$B and ^{12}C$(p, 2pp_s)\,^{10}$Be for the carbon beam momentum of 48 GeV/c with an outgoing nucleus in the ground or excited state with excitation energy up to about 6 MeV. The TISM allowed us to calculate the spectroscopic amplitude for a given quantum states of the NN pair and residual nucleus including the WF of their relative motion. The absorptive- and single-CEX ISI and FSI were taken into account in the eikonal approximation.

We found that absorption reduces the integrated cross section by more than an order of magnitude, while the CEX processes strongly increase the yield ratio ^{10}Be / ^{10}B. Absorption and CEX are very sensitive to the WF of the relative NN-B motion.

However, the effect of absorption on the shape of the studied distributions is very moderate, which was also found in Ref. [70], where the ISI and FSI effects were estimated within the framework of a diagrammatic approach for the same reactions. The strong effect of absorption was observed only for the angular distribution between the momentum of the outgoing nucleus ^{10}B and the relative momentum of the *pn* pair shown in Fig. 3(b).

The distributions of relative angles, missing momentum, and ^{10}B momentum measured by the BM@N Collaboration [19] are described quite well by the TISM irrespective of the choice of the WF of the relative *NN*-*B* motion when absorption is taken into account.

The present study is only the first attempt of a detailed comparison of the TISM with SRC data. In the future, the calculations can certainly be improved, in particular by including the [431] ^{13}P configuration of ^{12}C and a more accurate description of the ISI and FSI processes. Availability of more accurate data on SRCs in light nuclei (specific states of the residual nucleus, bigger statistics, differential cross sections) would be useful to further validate the TISM-based spectroscopic approach.

SRCs may also manifest themselves in a hard knock-out of nuclear clusters. A new theoretical analysis of the data [34,35] on the quasielastic knock-out of fast deuterons, using a similar method of taking into account the effects of ISI and FSI, would be useful. Of particular interest is the influence of SRCs on cumulative processes [71], where our model can also be applied.

ACKNOWLEDGMENTS

The authors are grateful to Dr. Maria Patsyuk for stimulating discussions and detailed explanations of the BM@N acceptance.

APPENDIX: CALCULATION OF THE FRACTIONAL PARENTAGE COEFFICIENTS OF THE TISM

The FPC of the TISM was calculated using Eq. (11). This equation contains the FPC of the conventional HO model and the cluster coefficient. In the case of $b = 2$, the latter is equal to the Talmi coefficient:

$$\langle p^2[f_X](\lambda_X\mu_X)\mathcal{L}S_XT_X|n\Lambda, 2N_X[f_X](\lambda_X\mu_X)L_XS_XT_X\rangle = \langle 11, 11 : \mathcal{L}|11|n\Lambda, N_XL_X : \mathcal{L}\rangle, \tag{A1}$$

where the notation of Ref. [30] is used in the r.h.s. The Talmi coefficients are tabulated in Ref. [30]. The same tabulation can also be found in Ref. [72].[10] The FPCs for transition to the ^{13}S and $^{13}D_I$ states (see Table I) are calculated as

$$\begin{aligned}
\mathrm{FPC}(^{13}S) &= (-1)^2 \times \left(\frac{12}{10}\right)^{2/2} \times \left(\frac{8}{2}\right)^{1/2} \times \left(\frac{12}{2}\right)^{-1/2} \\
&\quad \times \langle p^8[44](04)000|p^6[42](22)010; p^2[2](20)010\rangle \times \langle 11, 11 : 0|11|20, 00 : 0\rangle \\
&= \frac{6}{5} \times \left(\frac{7\times 8}{2}\right)^{1/2} \times \left(\frac{11\times 12}{2}\right)^{-1/2} \times \left[\sqrt{\frac{9}{14}} \times \left(-\sqrt{\frac{16}{54}}\right) \times \sqrt{\frac{1}{2}}\right] \times \sqrt{\frac{1}{2}} \\
&= -\sqrt{\frac{8}{275}},
\end{aligned} \tag{A2}$$

$$\begin{aligned}
\mathrm{FPC}(^{13}D_I) &= (-1)^2 \times \left(\frac{12}{10}\right)^{2/2} \times \left(\frac{8}{2}\right)^{1/2} \times \left(\frac{12}{2}\right)^{-1/2} \\
&\quad \times \langle p^8[44](04)000|p^6[42](22)2_I10; p^2[2](20)210\rangle \times \langle 11, 11 : 2|11|22, 00 : 2\rangle \\
&= \frac{6}{5} \times \left(\frac{7\times 8}{2}\right)^{1/2} \times \left(\frac{11\times 12}{2}\right)^{-1/2} \times \left[\sqrt{\frac{9}{14}} \times \left(-\sqrt{\frac{3}{54}}\right) \times \sqrt{\frac{1}{2}}\right] \times \sqrt{\frac{1}{2}} \\
&= -\sqrt{\frac{3}{550}},
\end{aligned} \tag{A3}$$

where the FPC of the conventional HO model is given by the product of three factors in the square brackets corresponding to the weight factor, orbital coefficient, and charge-spin coefficient tabulated in Ref. [47]. The FPC for transition to the $^{13}D_{II}$ state is obtained by replacing the orbital coefficient $-\sqrt{\frac{3}{54}} \to -\sqrt{\frac{35}{54}}$ in Eq. (A3). The FPCs for transitions to the ^{31}S, $^{31}D_I$, and $^{31}D_{II}$ states are obtained by replacing the charge-spin coefficient $\sqrt{\frac{1}{2}} \to -\sqrt{\frac{1}{2}}$ in the FPCs for transition to the ^{13}S, $^{13}D_I$, and $^{13}D_{II}$ states, respectively.

[10]Note that in Ref. [72] the main oscillator quantum number n is defined so that the number of oscillator quanta is $2n + l$, which differs from the definition of Ref. [30] used in our present work.

[1] C. Ciofi degli Atti, Phys. Rep. **590**, 1 (2015).
[2] O. Hen, G. A. Miller, E. Piasetzky, and L. B. Weinstein, Rev. Mod. Phys. **89**, 045002 (2017).
[3] E. Piasetzky, M. Sargsian, L. Frankfurt, M. Strikman, and J. W. Watson, Phys. Rev. Lett. **97**, 162504 (2006).
[4] I. Korover *et al.* (Lab Hall A Collaboration), Phys. Rev. Lett. **113**, 022501 (2014).
[5] A. Schmidt *et al.* (CLAS Collaboration), Nature (London) **578**, 540 (2020).
[6] A. Tang *et al.*, Phys. Rev. Lett. **90**, 042301 (2003).
[7] R. Shneor *et al.* (Jefferson Lab Hall A Collaboration), Phys. Rev. Lett. **99**, 072501 (2007).
[8] R. Subedi *et al.*, Science **320**, 1476 (2008).
[9] C. J. G. Onderwater *et al.*, Phys. Rev. Lett. **78**, 4893 (1997).
[10] C. J. G. Onderwater *et al.*, Phys. Rev. Lett. **81**, 2213 (1998).
[11] R. Starink *et al.*, Phys. Lett. B **474**, 33 (2000).
[12] G. Rosner, Prog. Part. Nucl. Phys. **44**, 99 (2000).
[13] C. Giusti, F. D. Pacati, K. Allaart, W. J. W. Geurts, W. H. Dickhoff, and H. Muther, Phys. Rev. C **57**, 1691 (1998).
[14] J. Ryckebusch, V. Van der Sluys, K. Heyde, H. Holvoet, W. Van Nespen, M. Waroquier, and M. Vanderhaeghen, Nucl. Phys. A **624**, 581 (1997).
[15] J. Ryckebusch and W. Van Nespen, Eur. Phys. J. A **20**, 435 (2004).
[16] C. Giusti, H. Muther, F. D. Pacati, and M. Stauf, Phys. Rev. C **60**, 054608 (1999).
[17] J. Ryckebusch, S. Janssen, W. Van Nespen, and D. Debruyne, Phys. Rev. C **61**, 021603(R) (2000).
[18] D. G. Middleton *et al.*, Eur. Phys. J. A **29**, 261 (2006).
[19] M. Patsyuk *et al.*, Nat. Phys. **17**, 693 (2021).
[20] R. B. Wiringa, Phys. Rev. C **73**, 034317 (2006).
[21] R. B. Wiringa, R. Schiavilla, S. C. Pieper, and J. Carlson, Phys. Rev. C **89**, 024305 (2014).
[22] M. Piarulli, S. Pastore, R. B. Wiringa, S. Brusilow, and R. Lim, Phys. Rev. C **107**, 014314 (2023).
[23] C. Colle, W. Cosyn, J. Ryckebusch, and M. Vanhalst, Phys. Rev. C **89**, 024603 (2014).
[24] J. Ryckebusch, W. Cosyn, S. Stevens, C. Casert, and J. Nys, Phys. Lett. B **792**, 21 (2019).
[25] J. Ryckebusch, W. Cosyn, T. Vieijra, and C. Casert, Phys. Rev. C **100**, 054620 (2019).
[26] R. Cruz-Torres, D. Lonardoni, R. Weiss, N. Barnea, D. W. Higinbotham, E. Piasetzky, A. Schmidt, L. B. Weinstein, R. B. Wiringa, and O. Hen, Nat. Phys. **17**, 306 (2021).
[27] R. Weiss, B. Bazak, and N. Barnea, Phys. Rev. Lett. **114**, 012501 (2015).
[28] R. Weiss, R. Cruz-Torres, N. Barnea, E. Piasetzky, and O. Hen, Phys. Lett. B **780**, 211 (2018).
[29] R. Weiss, B. Bazak, and N. Barnea, Phys. Rev. C **92**, 054311 (2015).
[30] V. G. Neudatchin and Y. F. Smirnov, *Nuklonnye Assotsiatsii v Legkikh Yadrakh (Nucleon Associations in Light Nuclei)* (Nauka, Moscow, 1969) [in Russian].
[31] V. Balashov, A. Boyarkina, and I. Rotter, Nucl. Phys. **59**, 417 (1964).
[32] A. N. Boyarkina, *Struktura yader 1p-obolochki (Structure of 1p-shell Nuclei)* [Moskovskij Gosudarstvennij Universitet (Moscow State University), Moscow, 1973] [in Russian].
[33] N. S. Chant, P. G. Roos, and C. W. Wang, Phys. Rev. C **17**, 8 (1978).
[34] D. Albrecht *et al.*, Nucl. Phys. A **338**, 477 (1980).
[35] J. Ero, Z. Fodor, P. Koncz, Z. Seres, M. Csatlos, B. A. Khomenko, N. N. Khovansky, Z. V. Krumshtein, Y. P. Merekov, and V. I. Petrukhin, Nucl. Phys. A **372**, 317 (1981).
[36] M. A. Zhusupov, O. Imambekov, and Y. N. Uzikov, Bull. Russ. Acad. Sci. Phys. **50**, 172 (1986).
[37] M. A. Zhusupov and Y. N. Uzikov, Fiz. Elem. Chastits At. Yadra **18**, 323 (1987).
[38] D. Albrecht *et al.*, Nucl. Phys. A **322**, 512 (1979).
[39] O. Imambekov and Y. N. Uzikov, Bull. Russ. Acad. Sci. Phys. **51**, 107 (1987).
[40] O. Imambekov, Y. N. Uzikov, and L. V. Shevchenko, Yad. Fiz. **44**, 1459 (1986).
[41] A. B. Larionov, A. Gillitzer, J. Haidenbauer, and M. Strikman, Phys. Rev. C **98**, 054611 (2018).
[42] Y. F. Smirnov and Y. M. Tchuvil'sky, Phys. Rev. C **15**, 84 (1977).
[43] Y. Uzikov and A. Uvarov, Phys. Part. Nucl. **53**, 426 (2022).
[44] D. Varshalovich, A. Moskalev, and V. Khersonskii, *Quantum Theory of Angular Momentum* (World Scientific, Singapore, 1988).
[45] H. A. Bethe and M. E. Rose, Phys. Rev. **51**, 283 (1937).
[46] J. P. Elliott and T. H. R. Skyrme, Proc. R. Soc. A **232**, 561 (1955).
[47] J. Elliott, J. Hope, and H. A. Jahn, Philos. Trans. R. Soc. A **246**, 241 (1953).
[48] A. A. Sakharuk and V. Zelevinsky, Phys. Rev. C **55**, 302 (1997).
[49] A. Sakharuk, V. Zelevinsky, and V. G. Neudatchin, Phys. Rev. C **60**, 014605 (1999).
[50] D. R. Tilley, J. H. Kelley, J. L. Godwin, D. J. Millener, J. E. Purcell, C. G. Sheu, and H. R. Weller, Nucl. Phys. A **745**, 155 (2004).
[51] L. L. Frankfurt, M. I. Strikman, and M. B. Zhalov, Phys. Rev. C **50**, 2189 (1994).
[52] A. B. Larionov and H. Lenske, Phys. Lett. B **773**, 470 (2017).
[53] R. T. Janus and I. E. McCarthy, Phys. Rev. C **10**, 1041 (1974).
[54] R. J. Glauber and G. Matthiae, Nucl. Phys. B **21**, 135 (1970).
[55] G. D. Alkhazov, G. M. Amalsky, S. L. Belostotsky, A. A. Vorobyov, O. A. Domchenkov, Y. V. Dotsenko, and V. E. Starodubsky, Phys. Lett. B **42**, 121 (1972).
[56] M. Duer *et al.* (CLAS Collaboration), Phys. Rev. Lett. **122**, 172502 (2019).
[57] R. Machleidt, Phys. Rev. C **63**, 024001 (2001).
[58] G. Fäldt and C. Wilkin, Phys. Lett. B **382**, 209 (1996).
[59] V. Lensky, V. Baru, J. Haidenbauer, C. Hanhart, A. E. Kudryavtsev, and U. G. Meissner, Eur. Phys. J. A **26**, 107 (2005).
[60] Y. Uzikov, Phys. Part. Nuclei **52**, 652 (2021).
[61] C. Ciofi degli Atti and S. Simula, Phys. Rev. C **53**, 1689 (1996).
[62] R. C. Kammerud, B. B. Brabson, R. R. Crittenden, R. M. Heinz, H. A. Neal, H. W. Paik, and R. A. Sidwell, Phys. Rev. D **4**, 1309 (1971).
[63] J. Cugnon, J. Vandermeulen, and D. L'Hote, Nucl. Instrum. Methods Phys. Res. B **111**, 215 (1996).
[64] M. Jain *et al.*, Phys. Rev. C **30**, 566 (1984).
[65] W. R. Gibbs and B. Loiseau, Phys. Rev. C **50**, 2742 (1994).

[66] C. Ciofi degli Atti, S. Simula, L. L. Frankfurt, and M. I. Strikman, Phys. Rev. C **44**, R7 (1991).
[67] G. Audi, A. H. Wapstra, and C. Thibault, Nucl. Phys. A **729**, 337 (2003).
[68] S. J. Brodsky and G. R. Farrar, Phys. Rev. Lett. **31**, 1153 (1973).
[69] V. A. Matveev, R. M. Muradian, and A. N. Tavkhelidze, Lett. Nuovo Cimento **7**, 719 (1973).
[70] Y. Uzikov, Acta Phys. Pol. Supp. **14**, 793 (2021).
[71] L. L. Frankfurt and M. I. Strikman, Phys. Lett. B **83**, 407 (1979).
[72] Y. F. Smirnov, Nucl. Phys. **27**, 177 (1961).